



## Supplementary Materials for

### **Loss of a satellite could explain Saturn's obliquity and young rings**

Jack Wisdom *et al.*

Corresponding author: Jack Wisdom, [wisdom@mit.edu](mailto:wisdom@mit.edu)

*Science* **377**, 1285 (2022)  
DOI: 10.1126/science.abn1234

#### **The PDF file includes:**

Materials and Methods  
Supplementary Text  
Figs. S1 to S5  
Table S1  
References

## Materials and Methods

### 1. Numerical integration of satellite systems

We have investigated several aspects of this problem with full numerical integrations of the dynamical evolution of Saturn satellite system. These integrations include Saturn, modelled as a rigid body, the gravitational moments of Saturn from  $J_2$  to  $J_6$ , the major satellites of Saturn, from Mimas to Iapetus, the Sun, and the four outer planets. Initial conditions and parameters are taken from JPL ephemerides DE440 and SAT440 (34, 35).

We use the symplectic n-body mapping method (36) to evolve the orbits of the system, the axisymmetric Lie-Poisson method (37) to evolve the rigid body motion of Saturn, and the symplectic corrector (38) to remove integrator induced oscillations. We use a universal Kepler solver (39) that can handle hyperbolic orbits.

We use hierarchical Jacobi coordinates (40) to effect the splitting of the n-body Hamiltonian into Keplerian and interaction parts. The hierarchical Jacobi coordinates are useful here to describe the motion of the satellites, which orbit Saturn, which in turn orbits the Sun, and interacts with the other planets. The Jacobi coordinates allow the separation of the center of mass from the relative motions of the other bodies. Each Jacobi coordinate specifies the rectangular coordinates of a body relative to the center of mass of bodies higher in the tree. The Jacobi coordinates have the property that the kinetic energy is quadratic in the velocities, as is the kinetic energy in barycentric coordinates. This allows a splitting of the  $n$ -body Hamiltonian into Keplerian, interaction, and center of mass coordinates.

All gravitational interactions are included; the system is fully coupled. The gravitational moments affect the motion of the satellites as well as the rotation of Saturn. The oblateness of Saturn ( $J_2$ ) interacting with the Sun affects Saturn's rotation (for example, inducing precession and nutation), as well as its orbit.

We use a stepsize that is  $\sim 15$  times smaller than the shortest period being integrated (38).

For the Saturnian satellites, Mimas has the smallest orbit period of about 23 hours. For most of our integrations we adopt a stepsize of 0.06 days (or 1.44 hours).

We monitor the energy and angular momentum error of our integrations. For a 50 Myr integration, without tidal friction, the relative energy error of the whole system grows irregularly and is  $\sim 5 \times 10^{-11}$ . The relative error in the angular momentum is of order  $2 \times 10^{-10}$ .

The detailed precessional motion of Saturn’s spin axis due to Solar System and planetary torques was independently verified by comparison of numerical integration results with trigonometric series representations of the pole direction provided by JPL. We also took account of the uncertainty in the instantaneous direction of Saturn’s pole at the J2000 epoch, determined from Cassini observations of Saturn’s rings (41), when computing our suite of numerical integrations.

2. Resonance model We construct a simple model that captures many aspects of the dynamics of the secular spin-orbit resonance with Neptune. This model can be used to interpret the results of the full numerical simulations. For a varying orbit, the dynamics is described by the averaged time-dependent Hamiltonian (8, 10, 42).

$$H = -\frac{1}{2}C\omega\alpha(\cos\epsilon)^2/(1-e^2)^{3/2}, \quad (\text{S1})$$

where  $\epsilon$  is the angle between the spin axis and the moving normal to the orbit, and  $e$  is Saturn’s orbital eccentricity. After expressing the Hamiltonian in terms of canonical coordinates that specify the orientation with respect to an inertial reference, the equations of motion are Hamilton’s equations (10, 42). The equations of motion are numerically integrated. We adopt the resonance locking expression for the evolution of the semimajor axis of Titan (14). The secular evolution of the orbit can be expressed as a sum of modes (43). Resonances occur if the precession frequency matches one of the mode frequencies.

A key feature of Eq. (2) is that the contribution from each satellite to  $q$ , the factor that is added to  $J_2$ , is proportional to the product of the mass of the satellite and the square of

its distance from the planet. The contribution of Titan to the precession constant dominates the contribution from  $J_2$ , and this contribution increases as Titan migrates outwards. Both Titan and Iapetus are sufficiently distant from Saturn that  $i^L$  is non-negligible. A Hamiltonian treatment that includes the precession constant as a parameter becomes inconsistent if there are distant satellites (13). Eq. (2) shows that the satellite contributions to the precession constant depend on the obliquity and the inclinations of the satellites to the Laplace plane. The obliquity varies, and so does the inclination to the Laplace plane, so actually the precession constant varies (13). This inconsistency is one reason why we have chosen to primarily investigate the evolution with full numerical integrations. Other investigations (12, 13) introduce additional approximations, for example, lumping all the other satellites into Titan. Nevertheless, the resonance model captures qualitative aspects of the dynamics.

### 3. Integration of unstable systems

Our integrations of the resonantly unstable systems require a smaller timestep, because there are close encounters. We can resolve an encounter by choosing a timestep that is near the orbital period of the satellite pair at a grazing distance, divided by 15. Applying this criterion to our systems, we have chosen a timestep of 0.0015 days (or 2.16 minutes). This is small, but the integrations of the unstable systems span less than 500 kyr. We find that with this stepsize, energy and angular momentum are conserved during encounters. The typical relative error in angular momentum at the end of these simulations is  $\sim 10^{-11}$ .

### 4. Tidal friction

If there is tidal friction, energy is no longer conserved but angular momentum is. For a given tidal model, we specify the rates  $da/dt$ ,  $(1/e)de/dt = \kappa_e$ , and  $(1/i)di/dt = \kappa_i$ , where  $a$ ,  $e$ , and  $i$  are the semimajor axis, eccentricity, and inclination to the equator of Titan's orbit, respectively, and  $\kappa_e$  and  $\kappa_i$  are the inverses of the timescales for eccentricity and inclination

damping. We additionally define  $\kappa_a = (1/a)da/dt$ .

Tidal friction is incorporated as velocity kicks. The magnitude of the kick is

$$\vec{k} = t_a \vec{v} + t_b \dot{r}(\hat{x} - (\dot{r}/v)\hat{v}) + t_g(\hat{p} \cdot \hat{v})(\hat{x} \times \vec{v}), \quad (\text{S2})$$

where  $\hat{x}$  is the direction of the relative vector  $\vec{x}$ ,  $\hat{v}$  is the direction of the relative velocity  $\vec{v}$ , and  $\hat{p}$  is the direction of the pole of the planet. The constants are  $t_a = \alpha_0 + e^2\alpha_1$ ,  $t_b = \beta + 4e^2\alpha_1$ , and  $t_g = \gamma$ , where  $e$  is the orbital eccentricity. Orbital inclinations damp to the Laplace plane. An angular momentum conserving kick is applied to the rotation. The constants  $\alpha_0$ ,  $\alpha_1$ ,  $\beta$ , and  $\gamma$  depend on the tidal model.

A rapid migration of Titan has been observed (14). This rapid migration is consistent with the resonance-locking theory of tidal evolution (44), in which the rate of evolution of oscillation modes in the planet controls the rate of satellite migration. For equilibrium tides, several terms in the tidal potential contribute to the evolution of the eccentricity (45). For resonance-locking tides, there is only a single term present, the 2200 term. In this case

$$\alpha_0 = \kappa_a/(2f) \quad (\text{S3})$$

$$\alpha_1 = (\kappa_e - (1/4)\kappa_a)/f \quad (\text{S4})$$

$$\beta = 2(\kappa_e - (1/4)\kappa_a) \quad (\text{S5})$$

$$\gamma = 2(\kappa_i - (1/4)\kappa_a) \quad (\text{S6})$$

where  $f = a(2/r - 1/a)$ , and  $r$  is the distance and  $a$  is the semimajor axis. These terms produce negligible evolution of the eccentricity and inclination, with a corresponding timescale of over 10 Gyr for Titan. For all practical purposes, the form for tidal friction that we adopt simply produces an evolution in semimajor axis.

For our tidally evolving simulations, we specify  $da/dt$  for Titan, but for simplicity ignore the tidal evolution of the other satellites. The measured rate of tidal evolution of Titan is  $11 \pm 2$

cm yr<sup>-1</sup> (radio tracking) and  $25.3 \pm 20.9$  cm yr<sup>-1</sup> (astrometry) (14); we explored the rates 7.33 cm yr<sup>-1</sup>, 10.00 cm yr<sup>-1</sup>, 12.22 cm yr<sup>-1</sup>, 13.75 cm yr<sup>-1</sup>, 15.71 cm yr<sup>-1</sup>, and 22.00 cm yr<sup>-1</sup>.

We also ignored eccentricity and inclination damping due to satellite tides. In some of our simulations Titan eccentricities and inclinations are larger than their present-day values. We expect modest damping of both  $e$  and  $i$  to occur due to satellite tides over the  $\sim 150$  Myr following excitation. Eccentricity damping depends on Titan's  $k_2/Q$ ; the measured potential Love number  $k_2$  is approximately 0.6, but only a lower bound on the dissipation parameter  $Q$  is available (46). A  $Q$  of  $\sim 60$  would be sufficient to damp Titan's eccentricity by a factor of two over 150 Myr. Inclination damping is probably dominated by obliquity tides in the subsurface ocean; the resulting damping timescale is  $\sim 300$  Myr (47), short enough that some damping should have occurred.

## Supplementary Text

### 1. Models of Saturn Interior and Angular Momentum Constraints

Here we present results from additional interior models. Our analysis relies on the result that high-precision spacecraft measurements of Saturn’s gravity harmonics  $J_2$ ,  $J_4$ , and  $J_6$  constrain the planet’s normalized angular momentum  $\mathcal{J}$  sufficiently tightly to exclude values at or above the critical value for resonance with Neptune,  $\mathcal{J}_c$ , where we find that  $\mathcal{J}_c$  lies in the small range  $0.087360 - 0.087395$ . Some values of  $\mathcal{J}$  permitted by the gravity harmonics lie as close as 0.5% below  $\mathcal{J}_c$ , but here we verify that modeling uncertainties do not eliminate this gap. Saturn’s axial precession is currently not in resonance with Neptune.

The published  $J_2$ ,  $J_4$ , and  $J_6$  are normalized to  $R_e = 60330$  km, whereas our interior models are matched to values normalized to the observed 1-bar radius,  $R_e = 60268$  km. All normalizations in our calculations are consistent with the latter number.

In Fig. S2, we plot the probability density of permitted angular momentum values that result from ensembles of models with four constant-density spheroids that a) match only  $J_2$ , b) match  $J_2$  and  $J_4$ , or c) match  $J_2$ ,  $J_4$ , as well as  $J_6$ . If only  $J_2$  is matched, angular momentum values above the critical value are permitted. Already if  $J_4$  is added to constrain the models, angular momentum values near or above the critical value are excluded. If  $J_6$  is introduced as a model constraint, lower angular momentum values are excluded also. All these calculations were performed with the CMS method using four spheroids. The equatorial radii and the density of the three inner spheroids were allowed to vary. The shapes of the spheroids were adjusted until they represented equipotential surfaces. Then the gravity harmonics and angular momentum were derived. No effects from differential rotation were included. In Fig. S2, we report results of a single rotation period of 10:33:34 h while Fig. 1 shows results over a range of periods.

In Fig. S3, we show the probability density of angular momentum from CMS calculations with 6, 8, 10, 15, and 20 spheroids. We find that increasing the number of spheroids does not

enable us to construct models that yield larger angular momenta while matching the observed gravity harmonics  $J_2$ ,  $J_4$ , and  $J_6$ . To reduce the parameter space, we constrained the equatorial spheroid radii to reside on the linear grid in radius rather than allowing them to be varied as we did in our four-spheroid models in Fig. S2.

In Fig. S4, we show the probability density of angular momentum for models matching four different  $J_6$  values while matching the measured values of  $J_2$  and  $J_4$ . The figure shows that an assumed decrease in  $J_6$  corresponds to a decrease in the likely angular momentum, and larger changes in  $J_6$  correspond to larger changes in the likely angular momentum. We find that the models without differential rotation in Fig. 1 represent an upper bound to the inferred angular momentum. Every model ensemble includes assumptions and approximations. But if, for a given set of assumptions, differential rotation is introduced to an ensemble, the inferred angular momentum is reduced. This shifts the angular momentum farther away from the critical value, which again supports our conclusion that Saturn is not in resonance with Neptune today. This argument rests on the following points:

1. Fig. 1 shows that models with differential rotation predict smaller angular momenta than models that match  $J_2$ ,  $J_4$ , and  $J_6$  without it.
2. Fig. S1 shows that the effects of differential rotation increase the higher-order gravity harmonics. The increase of  $J_6$  is approximately  $6 \times 10^{-6}$ .
3. In our Saturn models that include differential rotation, most of the contribution to  $J_6$  comes from the interior but there is also a positive contribution from the differential rotation. The latter term reduces the contribution to  $J_6$  from the interior to below the equivalent value from a model without differential rotation, in which the entire  $J_6$  contribution comes from the interior.
4. A reduced contribution to  $J_6$  from the interior leads to a reduction of the angular momen-



tum as we show in Fig. S4. Therefore models invoking differential rotation to contribute a fraction to  $J_6$ , predict smaller angular momenta than models without differential rotation, which yield an upper bound to the inferred angular momentum. This is consistent with the results in Fig. 1.

## 2. Orbital resonances encountered

As the system is evolved backwards in time, two principal orbital resonances are encountered, which have been previously studied: the 5:1 mean motion Titan-Iapetus resonance (in which the orbital period of Iapetus is approximately five times the orbital period of Titan) (48), and a complicated secular resonance involving the orbit of Iapetus, the longitude of the equator of Saturn, and the longitude of the perihelion of Jupiter (26). The resonant argument of this secular resonance is  $\varpi - \varpi_J + \Omega - \Omega_{\text{eq}}$ , where  $\varpi$  and  $\Omega$  are the longitudes of the pericenter and ascending node of Iapetus,  $\varpi_J$  is the longitude of the pericenter of Jupiter, and  $\Omega_{\text{eq}}$  is the longitude of the equator of Saturn. Another orbital resonance that affects the backward evolutions is the 7:2 mean motion Rhea-Titan resonance, with resonant argument  $7\lambda_T - 2\lambda_R - \varpi_R - 4\varpi_T$ , where  $\lambda_T$  and  $\lambda_R$  are the mean longitudes of Titan and Rhea, respectively, and  $\varpi_T$  and  $\varpi_R$  are the longitudes of their pericenters.

None of these resonances affects the precession constant enough for the system to leave the Neptune spin-orbit precession resonance.

## 3. Disruption Radius

The outer edge of the A-ring, the outermost of Saturn's main rings, is around  $2.3R_e$ ; for a density of  $1 \text{ g cm}^{-3}$  the distance from the planet at which a body without strength or viscosity is pulled apart is around  $2.1R_e$  (49). The distance below which disruption occurs is uncertain. Bodies with finite viscosity (50) or internal shear strength (51) may experience disruption at somewhat smaller distances.

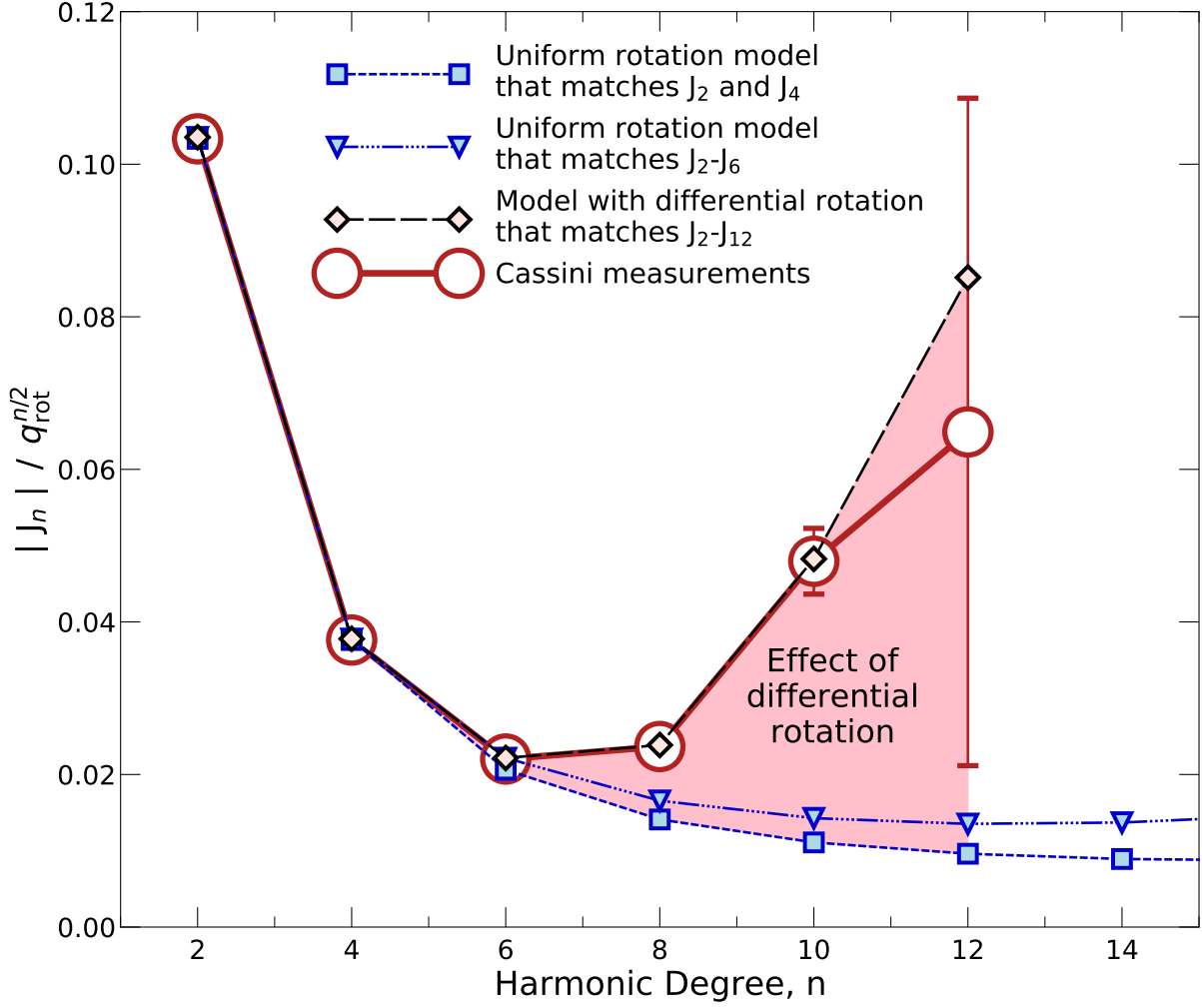


Figure S1: **The gravitational moments,  $J_n$ , versus degree.** The interior models with differential rotation fit the observed moments up to  $J_{12}$  within their errors. All moments have been scaled by powers of the rotational parameter  $q_{\text{rot}} = \omega^2 R_e^3 / GM$ . See (18). Moments of a model that match  $J_2$  and  $J_4$  with uniform rotation (blue dashed curve with blue boxes), a model that matches  $J_2$ ,  $J_4$ , and  $J_6$  with uniform rotation (blue dot-dashed curve with blue triangles), a model that matches  $J_2 - J_{12}$  with differential rotation (dashed black line with yellow diamonds), with Cassini measurements and errors (red curve with red circles). The effect of differential rotation is shaded light red.

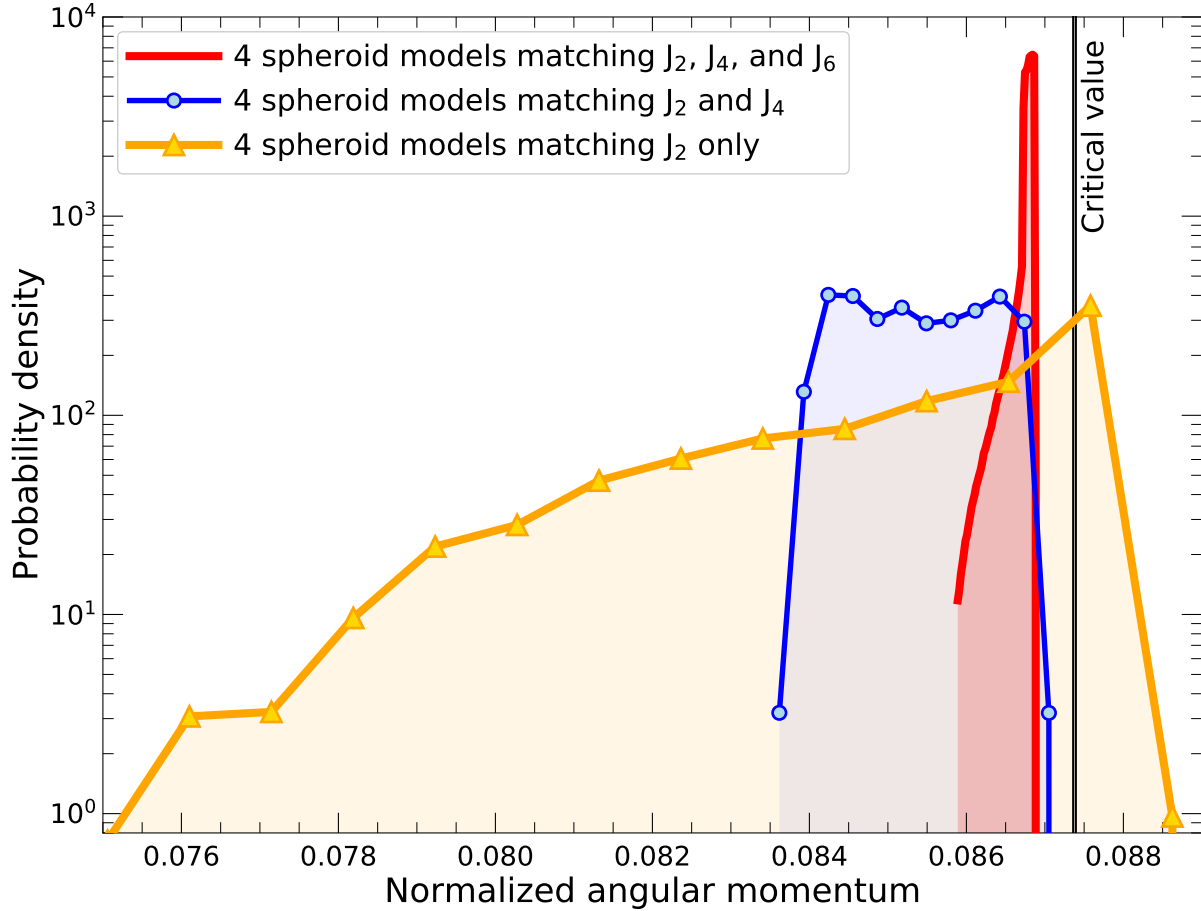


Figure S2: **Probability density of model predictions for the normalized angular momentum.** Ensembles of models that match the gravity harmonic  $J_2$  only (orange curve and orange triangles), match  $J_2$  and  $J_4$  (blue curve and blue circles), or match all three harmonics  $J_2$ ,  $J_4$ , and  $J_6$  (red curve). Only with models that solely match  $J_2$  is it possible to obtain angular momentum values around or above the critical value (grey band between the vertical black lines).  $J_2$  and  $J_4$  together constrain the moment of inertia sufficiently well to exclude values near the critical value.  $J_6$  narrows the range of permitted angular momentum values further by excluding low values. All calculations were performed for a rotation period of 10:33:34 h with the CMS method using four spheroids.

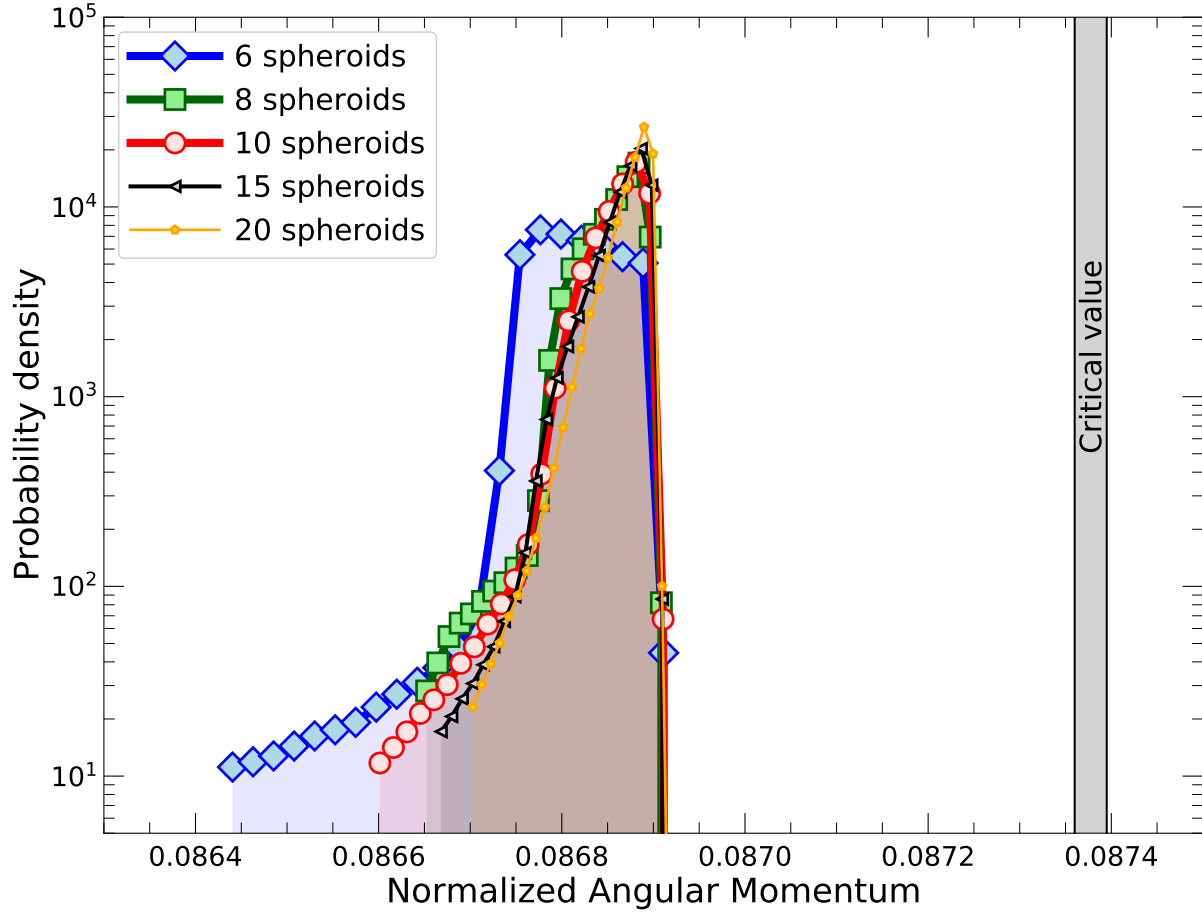


Figure S3: **Probability density of model predictions for the normalized angular momentum.** Ensembles of models with 6 spheroids (blue curve with blue diamonds), 8 spheroids (green curve with green squares), 10 spheroids (red curve with red circles), 15 spheroids (black curve with black triangles), and 20 spheroids (orange curve with orange dots) that match the observed gravity harmonics  $J_2$ ,  $J_4$ , and  $J_6$ . The diagram shows that adding additional spheroids to the models does not enable one to approach the critical angular momentum value (vertical grey band). All calculations were performed with the CMS method without differential rotation for a rotation period of 10:33:34 h.

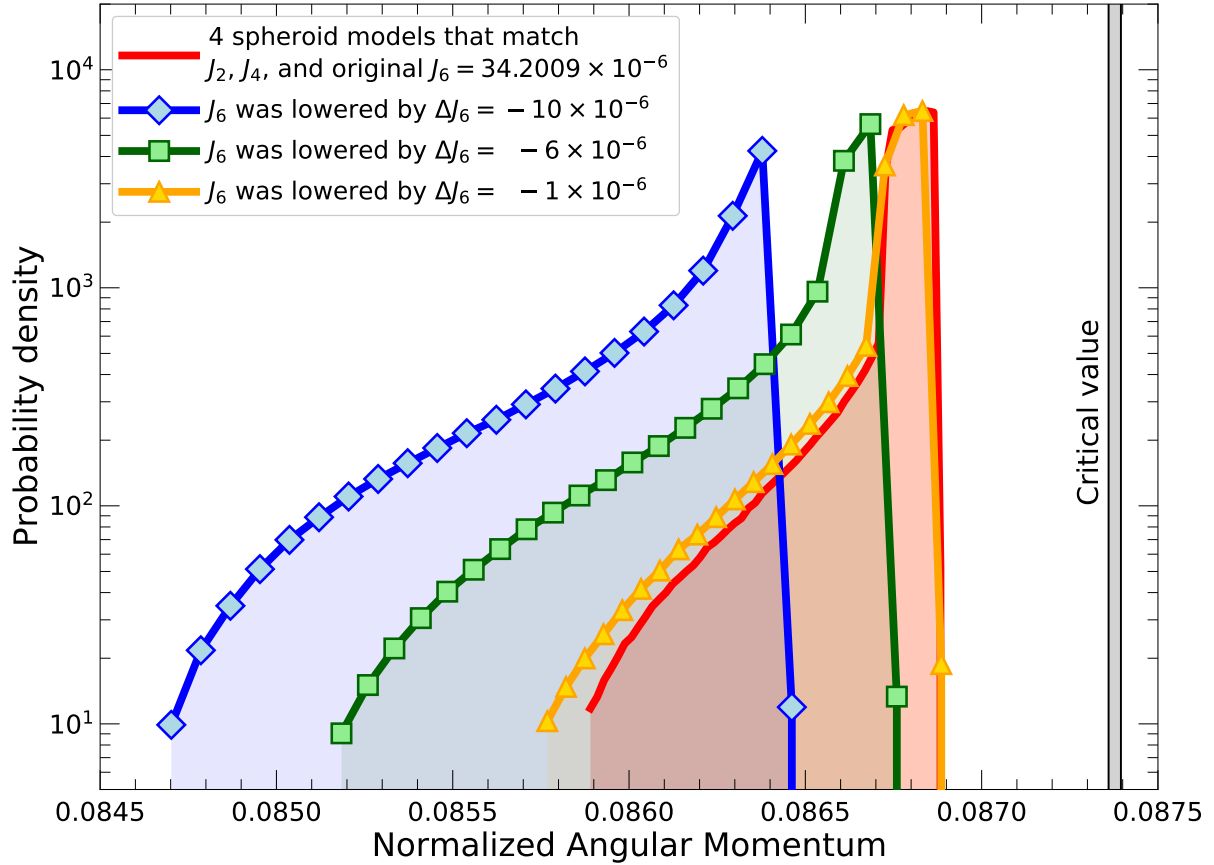


Figure S4: **Probability density of model predictions for the normalized angular momentum.** Ensembles of models that match the observed gravity harmonics  $J_2$ ,  $J_4$ , and four different values of  $J_6$  (original (red curve), lowered by  $-1 \times 10^{-6}$  (orange curve and orange triangles), lowered by  $-6 \times 10^{-6}$  (green curve with green boxes), lowered by  $-10 \times 10^{-6}$  (blue curve with blue diamonds)). There is a correlation between the  $J_6$  value and the inferred angular momentum. All calculations were performed without differential rotation for a rotation period of 10:33:34 h with the CMS method using four spheroids.

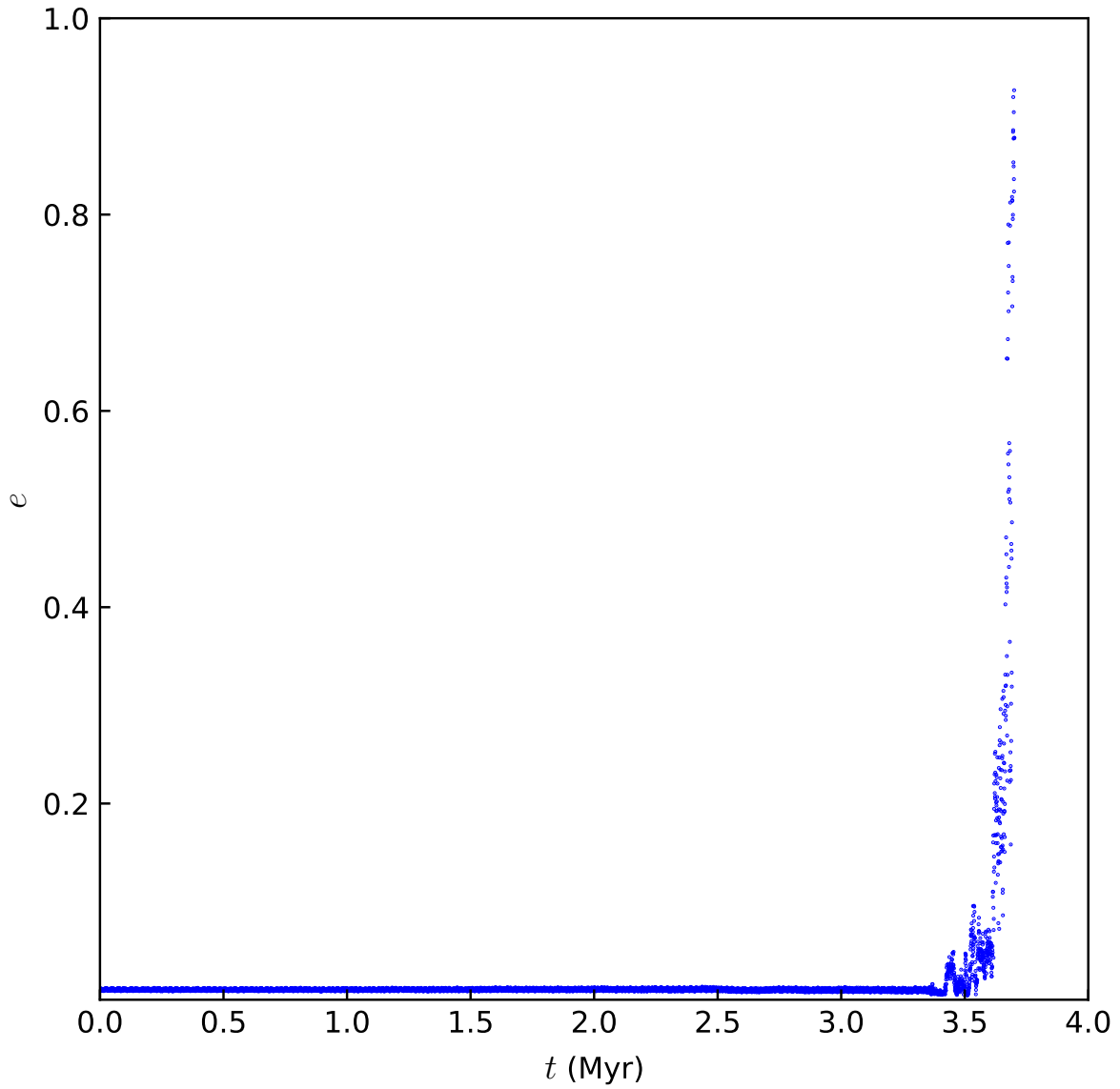


Figure S5: **Eccentricity of Chrysalis as a function of time.** A simulation in which the system encounters the 3:1 Titan-Chrysalis resonance as Titan tidally migrated outwards. The orbit of Chrysalis becomes chaotic and the eccentricity rapidly becomes large enough for encounters with the other satellites. This simulation included Hyperion.

Table S1: **Values of Saturn's normalized angular momentum of Saturn in Fig. 1.**

Method	Rotation Period (s)	Normalized Angular Momentum
CMS method with DR	37800	0.08662998
	37964	0.08654830
	38014	0.08651077
	38362	0.08636567
	38745	0.08609887
	38826	0.08605070
CMS method without DR	37800	0.08701761
	37964	0.08693018
	38014	0.08690372
	38362	0.08671972
	38745	0.08652001
	38826	0.08647747
CLC method without DR	37782	0.08700588
	37927	0.08692498
	38074	0.08684816
	38222	0.08676730
	38372	0.08668612
	38523	0.08661436
	38676	0.08653295
	38831	0.08645762
Four-spheroid CMS model without DR	38014	0.08678220
	38362	0.08660454
	38725	0.08639766

## References and Notes

1. W. R. Ward, D. P. Hamilton, Tilting Saturn. I. Analytic model. *Astrophys. J.* **128**, 2501–2509 (2004).
2. P. Goldreich, S. Tremaine, The dynamics of planetary rings. *Annu. Rev. Astron. Astrophys.* **20**, 249–283 (1982). [doi:10.1146/annurev.aa.20.090182.001341](https://doi.org/10.1146/annurev.aa.20.090182.001341)
3. Z. Zhang, A. G. Hayes, M. A. Janssen, P. D. Nicholson, J. N. Cuzzi, I. de Pater, D. E. Dunn, Exposure age of Saturn’s A and B rings, and the Cassini Division as suggested by their non-icy material content. *Icarus* **294**, 14–42 (2017). [doi:10.1016/j.icarus.2017.04.008](https://doi.org/10.1016/j.icarus.2017.04.008)
4. L. Iess, B. Militzer, Y. Kaspi, P. Nicholson, D. Durante, P. Racioppa, A. Anabtawi, E. Galanti, W. Hubbard, M. J. Mariani, P. Tortora, S. Wahl, M. Zannoni, Measurement and implications of Saturn’s gravity field and ring mass. *Science* **364**, eaat2965 (2019). [doi:10.1126/science.aat2965](https://doi.org/10.1126/science.aat2965) [Medline](#)
5. A. Crida, S. Charnoz, H.-W. Hsu, L. Dones, Are Saturn’s rings actually young? *Nat. Astron.* **3**, 967–970 (2019). [doi:10.1038/s41550-019-0876-y](https://doi.org/10.1038/s41550-019-0876-y)
6. A. W. Harris, W. R. Ward, Dynamical constraints on the formation and evolution of planetary bodies. *Annu. Rev. Earth Planet. Sci.* **10**, 61–108 (1982). [doi:10.1146/annurev.ear.10.050182.000425](https://doi.org/10.1146/annurev.ear.10.050182.000425)
7. G. Cassini, *Traite de L’origine ede Progres de L’Astronomie* (Paris, 1693).
8. S. J. Peale, Generalized Cassini’s laws. *Astron. J.* **74**, 483–489 (1969). [doi:10.1086/110825](https://doi.org/10.1086/110825)
9. J. Laskar, P. Robutel, The chaotic obliquity of the planets. *Nature* **361**, 608–612 (1993). [doi:10.1038/361608a0](https://doi.org/10.1038/361608a0)
10. J. Touma, J. Wisdom, The chaotic obliquity of Mars. *Science* **259**, 1294–1297 (1993). [doi:10.1126/science.259.5099.1294](https://doi.org/10.1126/science.259.5099.1294) [Medline](#)
11. W. R. Ward, Past orientation of the lunar spin axis. *Science* **189**, 377–379 (1975). [doi:10.1126/science.189.4200.377](https://doi.org/10.1126/science.189.4200.377) [Medline](#)
12. M. Saillenfest, G. Lari, G. Boué, The large obliquity of Saturn explained by the fast migration of Titan. *Nat. Astron.* **5**, 345–349 (2021). [doi:10.1038/s41550-020-01284-x](https://doi.org/10.1038/s41550-020-01284-x)
13. M. Saillenfest, G. Lari, G. Boué, A. Courtot, The past and future obliquity of Saturn as Titan migrates. *Astron. Astrophys.* **647**, A92 (2021). [doi:10.1051/0004-6361/202039891](https://doi.org/10.1051/0004-6361/202039891)
14. V. Lainey, L. G. Casajus, J. Fuller, M. Zannoni, P. Tortora, N. Cooper, C. Murray, D. Modenini, R. S. Park, V. Robert, Q. Zhang, Resonance locking in giant planets indicated by the rapid orbital expansion of Titan. *Nat. Astron.* **4**, 1053–1058 (2020). [doi:10.1038/s41550-020-1120-5](https://doi.org/10.1038/s41550-020-1120-5)
15. G. F. Lindal, D. N. Sweetnam, V. R. Eshleman, The atmosphere of Saturn—An analysis of the Voyager radio occultation measurements. *Astron. J.* **90**, 1136–1146 (1985). [doi:10.1086/113820](https://doi.org/10.1086/113820)
16. B. Militzer, W. B. Hubbard, Ab initio equation of state for hydrogen-helium mixtures with recalibration of the giant-planet mass-radius relation. *Astrophys. J.* **774**, 148 (2013). [doi:10.1088/0004-637X/774/2/148](https://doi.org/10.1088/0004-637X/774/2/148)



17. W. B. Hubbard, Concentric Maclaurin spheroid models of rotating liquid planets. *Astrophys. J.* **768**, 43 (2013). [doi:10.1088/0004-637X/768/1/43](https://doi.org/10.1088/0004-637X/768/1/43)
18. B. Militzer, S. Wahl, W. B. Hubbard, Models of Saturn's interior constructed with an accelerated concentric Maclaurin spheroid method. *Astrophys. J.* **879**, 78 (2019). [doi:10.3847/1538-4357/ab23f0](https://doi.org/10.3847/1538-4357/ab23f0)
19. J. Wisdom, W. B. Hubbard, Differential rotation in Jupiter: A comparison of methods. *Icarus* **267**, 315–322 (2016). [doi:10.1016/j.icarus.2015.12.030](https://doi.org/10.1016/j.icarus.2015.12.030)
20. W. B. Hubbard, Gravitational signature of Jupiter's deep zonal flows. *Icarus* **137**, 357–359 (1999). [doi:10.1006/icar.1998.6064](https://doi.org/10.1006/icar.1998.6064)
21. Materials and methods are provided in the supplementary materials.
22. S. Tremaine, On the origin of the obliquities of the outer planets. *Icarus* **89**, 85–92 (1991). [doi:10.1016/0019-1035\(91\)90089-C](https://doi.org/10.1016/0019-1035(91)90089-C)
23. R. Brasser, M. H. Lee, Tilting Saturn without tilting Jupiter: Constraints on giant planet migration. *Astron. J.* **150**, 157 (2015). [doi:10.1088/0004-6256/150/5/157](https://doi.org/10.1088/0004-6256/150/5/157)
24. S. Tremaine, J. Touma, F. Namouni, Satellite dynamics on the Laplace surface. *Astron. J.* **137**, 3706–3717 (2009). [doi:10.1088/0004-6256/137/3/3706](https://doi.org/10.1088/0004-6256/137/3/3706)
25. W. Polycarpe, M. Saillenfest, V. Lainey, A. Vienne, B. Noyelles, N. Rambaux, Strong tidal energy dissipation in Saturn at Titan's frequency as an explanation for Iapetus orbit. *Astron. Astrophys.* **619**, A133 (2018). [doi:10.1051/0004-6361/201833930](https://doi.org/10.1051/0004-6361/201833930)
26. M. Čuk, L. Dones, D. Nesvorný, K. J. Walsh, Secular resonance between Iapetus and the giant planets. *Mon. Not. R. Astron. Soc.* **481**, 5411–5421 (2018).
27. L. Dones, A recent cometary origin for Saturn's rings? *Icarus* **92**, 194–203 (1991). [doi:10.1016/0019-1035\(91\)90045-U](https://doi.org/10.1016/0019-1035(91)90045-U)
28. A. T. Sinclair, On the origin of the commensurabilities amongst the satellites of Saturn. *Mon. Not. R. Astron. Soc.* **160**, 169–187 (1972). [doi:10.1093/mnras/160.2.169](https://doi.org/10.1093/mnras/160.2.169)
29. C. Sagan, S. F. Dermott, The tide in the seas of Titan. *Nature* **300**, 731–733 (1982). [doi:10.1038/300731a0](https://doi.org/10.1038/300731a0)
30. G. Tobie, J. I. Lunine, C. Sotin, Episodic outgassing as the origin of atmospheric methane on Titan. *Nature* **440**, 61–64 (2006). [doi:10.1038/nature04497](https://doi.org/10.1038/nature04497) [Medline](https://pubmed.ncbi.nlm.nih.gov/16411111/)
31. R. Hyodo, S. Charnoz, K. Ohtsuki, H. Genda, Ring formation around giant planets by tidal disruption of a single passing large Kuiper belt object. *Icarus* **282**, 195–213 (2017). [doi:10.1016/j.icarus.2016.09.012](https://doi.org/10.1016/j.icarus.2016.09.012)
32. J. Wisdom, R. Dbouk, B. Militzer, W. B. Hubbard, F. Nimmo, B. G. Downey, R. G. French, SaturnObliquityRings, Harvard Dataverse Repository (2022); <https://doi.org/10.7910/DVN/RJZXGW>.
33. J. Wisdom, NbodySatellites, Zenodo (2022); <https://doi.org/10.5281/zenodo.6960630>.
34. Jet Propulsion Laboratory, California Institute of Technology, NAIF, Planetary Data System Navigation Node; <ftp://ssd.jpl.nasa.gov/pub/eph/planets/bsp/de440.bsp>.

35. Jet Propulsion Laboratory, California Institute of Technology, NAIF, Planetary Data System Navigation Node; <ftp://ssd.jpl.nasa.gov/pub/eph/satellites/bsp/sat4401.bsp>.
36. J. Wisdom, M. Holman, Symplectic maps for the N-body problem. *Astron. J.* **102**, 1528–1538 (1991). [doi:10.1086/115978](https://doi.org/10.1086/115978)
37. J. Touma, J. Wisdom, Lie-Poisson integrators for rigid body dynamics in the solar system. *Astron. J.* **107**, 1189 (1994). [doi:10.1086/116931](https://doi.org/10.1086/116931)
38. J. Wisdom, M. Holman, J. Touma, Symplectic correctors. *Fields Inst. Commun.* **10**, 217 (1996).
39. J. Wisdom, D. M. Hernandez, A fast and accurate universal Kepler solver without Stumpff series. *Mon. Not. R. Astron. Soc.* **453**, 3015–3023 (2015). [doi:10.1093/mnras/stv1862](https://doi.org/10.1093/mnras/stv1862)
40. G. J. Sussman, J. Wisdom, *Structure and Interpretation of Classical Mechanics* (MIT Press, ed. 2, 2014).
41. R. G. French, C. A. McGhee-French, K. Loneragan, T. Sepersky, R. A. Jacobson, P. D. Nicholson, M. M. Hedman, E. A. Marouf, J. E. Colwell, Noncircular features in Saturn's rings IV: Absolute radius scale and Saturn's pole direction. *Icarus* **290**, 14–45 (2017). [doi:10.1016/j.icarus.2017.02.007](https://doi.org/10.1016/j.icarus.2017.02.007)
42. J. Wisdom, Dynamics of the lunar spin axis. *Astron. J.* **131**, 1864–1871 (2006). [doi:10.1086/499581](https://doi.org/10.1086/499581)
43. J. H. Applegate, M. R. Douglas, Y. Gursel, G. J. Sussman, J. Wisdom, The outer solar system for 200 million years. *Astron. J.* **92**, 176–194 (1986). [doi:10.1086/114149](https://doi.org/10.1086/114149)
44. J. Fuller, J. Luan, E. Quataert, Resonance locking as the source of rapid tidal migration in the Jupiter and Saturn moon systems. *Mon. Not. R. Astron. Soc.* **458**, 3867–3879 (2016). [doi:10.1093/mnras/stw609](https://doi.org/10.1093/mnras/stw609)
45. W. M. Kaula, Tidal dissipation by solid friction and the resulting orbital evolution. *Rev. Geophys.* **2**, 661–685 (1964). [doi:10.1029/RG002i004p00661](https://doi.org/10.1029/RG002i004p00661)
46. D. Durante, D. J. Hemingway, P. Racioppa, L. Iess, D. J. Stevenson, Titan's gravity field and interior structure after Cassini. *Icarus* **326**, 123–132 (2019). [doi:10.1016/j.icarus.2019.03.003](https://doi.org/10.1016/j.icarus.2019.03.003)
47. B. G. Downey, F. Nimmo, I. Matsuyama, Inclination damping on Callisto. *Mon. Not. R. Astron. Soc.* **499**, 40–51 (2020). [doi:10.1093/mnras/staa2802](https://doi.org/10.1093/mnras/staa2802)
48. W. Polycarpe, V. Lainey, A. Vienne, B. Noyelles, M. Saillenfest, N. Rambaux, in vol. 49 of *AAS/Division of Dynamical Astronomy Meeting* (American Astronomical Society, 2018), p. 9.
49. E. Roche, Académie des sciences et lettres de montpellier. *Mém. Sect. Sci* **1**, 243–262 (1847).
50. S. Sridhar, S. Tremaine, Tidal disruption of viscous bodies. *Icarus* **95**, 86–99 (1992). [doi:10.1016/0019-1035\(92\)90193-B](https://doi.org/10.1016/0019-1035(92)90193-B)
51. A. R. Dobrovolskis, Tidal disruption of solid bodies. *Icarus* **88**, 24–38 (1990). [doi:10.1016/0019-1035\(90\)90175-9](https://doi.org/10.1016/0019-1035(90)90175-9)